The International Journal of Advanced Manufacturing Technology (2023) 126:4873–4889
https://doi.org/10.1007/s00170-023-10953-w

ORIGINAL ARTICLE

Analytical and experimental investigation on the distribution of solidification crack initiation sites throughout a laser spot weld

Mohsen Sheikhi[1] · Zeinab Malekshahi Beiranvand[2] · F. Malek Ghaini[2] · Michael J. Benoit[3]

Received: 20 September 2022 / Accepted: 19 January 2023 / Published online: 24 February 2023

Abstract

The objective of this this study is to investigate the distribution of crack initiation sites in the unsteady solidification conditions of pulsed laser welding for an AA2024 aluminum alloy, using both analytical and experimental methods. The employed analytical model considers the competition between volume change rate and liquid flow rate during the final stages of solidification. The former has a direct relationship with solidification rate (r), the latter has an inverse relationship with the length of the crack-vulnerable zone (l), and the risk of cracking decreases with lower values of $r \times l$. According to this model, the distribution of crack initiation sites is more strongly influenced by the solidification rate profile, specifically the solidification rate at the fusion line (r_{FL}) and at the weld center (r_{WC}). The crack initiation site will move toward the weld center as (r_{WC}-r_{FL})/r_{FL} increases. The model states that in square-wave pulse welded samples, a decrease in r_{FL} caused by preheating causes crack initiation sites to move from the FL toward the WC and crack severity to decrease. Moreover, it was shown that ramp down pulse shaping was more effective at reducing cracks, as both r and l can be controlled and, in turn, $r \times l$ can be reduced enough to prevent crack initiation. The model's reliability was assessed using experimental pulsed laser welding tests that considered the influence of base metal preheating and temporal ramp down pulse shaping.

Keywords Aluminum welding · Laser welding · Solidification cracking · Hot tearing · Crack initiation · Crack distribution

1 Introduction

Heat treatable aluminum alloys are widely used in several industries due to their high strength to weigh ratio, particularly after relatively simple heat treatments, but the application of these alloys has been limited in some applications due to challenges encountered in fusion welding processes. Most of heat treatable aluminum alloys, especially the AA2xxx series aluminum alloys, are known to be susceptible to hot cracking during fusion welding, which leads to a significant decrease in the mechanical properties of the welded joint [1–5]. This problem has been attributed to wide solidification temperature range, relatively high thermal expansion coefficient, and large solidification shrinkage of these alloys [5–8]. One of the most common approaches to eliminate solidification cracking during welding of heat treatable aluminum alloys is through the use of a 4xxx or 5xxx filler metal, which results in a fusion zone composition that is resistant to solidification cracking. However, this solution may decrease the feasibility of some applications, such as laser spot welding. Laser spot welding is a non-contact welding technology that has promising potential as a fusion welding process due to the high accuracy in process control, precise heat input, narrow heat affected zone, and minimal thermal distortion [8–11].

It has been reported that the susceptibility to solidification cracking can be significantly decreased when ramp down control is used in pulsed laser welding (compared to a square-wave pulse) [11]. However, the crack mechanisms, variation of solidification characteristic such as the thermal gradient (G) and solidification rate (r) and, consequently, the variation of crack initiation sites, are less well understood for non-steady welding processes. A robust and comprehensive model should be able to accurately forecast the distribution of cracking initiation sites throughout the entire weld pool. This work aims to

✉ Mohsen Sheikhi
sheikhi.mohsen@basu.ac.ir

[1] Department of Materials Engineering, Bu-Ali Sina University, Hamedan 65178-38695, Iran

[2] Department of Materials Engineering, Tarbiat Modares University, Tehran 14115-143, Iran

[3] School of Engineering, University of British Columbia, Kelowna, Canada

find an explanation for why altering welding parameters and, consequently, the solidification characteristics, leads to a variable distribution of crack initiation sites in weld pool.

Several models and criteria with differing capabilities are presently used to predict solidification crack susceptibility. The first type of criteria qualitatively ranks the relative susceptibility of an alloy to solidification cracking (i.e., a susceptibility index). These types of models do not prescribe a critical value for when cracking will occur. The criteria proposed by Kou [12] and Easton et al. [13] fall into this category. The second type of criteria aims at predicting the critical condition for crack formation, and includes the Rappaz-Drezet-Gremaud (RDG) [14], Braccini [15], and Suyitno-Katgerman-Kool (SKK) models [16]. In these models, a critical value for one parameter is proposed (e.g., strain rate) which, if exceeded, will lead to crack formation.

Recently, Sheikhi et al. [17] developed a simple model that proposed a new critical condition for cracking and, therefore, falls in the second type of criteria. This model is able to predict the actual cracking by taking both material properties and the process conditions in to account. The objective of the current study is to modify this model to account for non-equilibrium conditions at the solid/liquid interface during rapid solidification and to evaluate the capability of this approach to accurately predict the location of crack initiation sites in the non-equilibrium and non-steady state conditions of pulsed laser welding of aluminum alloy AA2024. The proposed model accounts for the competition between volume change rate and liquid flow rate in the mushy state and rapid solidification effects. Laser spot welds experiments in which the substrate pre-heat and temporal pulse shaping were used to validate the model predictions.

2 Methods

2.1 Experiments

AA2024 sheet in the fully annealed condition (O temper) with dimension of $60 \times 50 \times 2$ mm^3 was used as base metal in this investigation. The measured chemical composition of this alloy is presented in the Table 1. Bead-on-plate single spot laser welding was employed in this investigation. An IQL-10 pulsed Nd:YAG laser machine with an optical lens (75×10^{-3} m focal length) and square-wave pulse was used for welding. This laser source is able to produce combinations of pulse durations and frequencies from 2×10^{-4} to 2×10^{-2} s and 1 to 1000 Hz respectively, but it is limited to an average power of 400 W. A 5000W-LP model power meter was used for measuring the laser power during welding. Argon shielding gas was used for all experiments at a flow rate of 10 l per minute.

The effect of base metal pre-heat temperature on solidification cracking in the laser melt pool was studied by performing welds on sheets at room temperature and 300 °C. Preheating was performed by electric heater placed bottom of the samples, and the base metal temperature was set at 300 ± 5 °C using temperature controller thermocouple. To reduce the effect of weld pool geometry on cracking, the laser pulse energies were selected according to the base metal initial temperature and prior experimental results [17], such that similar weld pool profiles were obtained for both room temperature and 300 °C. The resultant laser welding parameters for each base metal temperature necessary to maintain constant weld pool geometry are given in Table 2. The pulse frequency and pulse duration were kept constant for all experiments and were equal to 12 Hz and 5 ms, respectively. The laser beam diameter at the focal point was 500 µm.

After welding, the top surface and cross sections of the weld samples were polished and then etched with Keller's solution. The number of crack initiation sites was counted using optical microscopy at five equal intervals between the fusion line (FL) and the weld pool's center at 200 × magnification. The number of cracks was counted on both the top surface and cross section of ten spot welds for both base metal temperatures. A solidification cracking index ($SCI_{(x_2-x_1)}$) in the interval (x_2-x_1) of the weld pool was defined as the proportion of crack initiation sites found within the given interval relative to the total number of cracks in spot section, i.e., $SCI_{(x_2-x_1)} = \frac{\text{Number of crack at distance of } (x_2-x_1)}{\text{Total crack numbers in the spot}} \times 100$.

Table 2 Pulsed laser welding parameters used for each base metal temperature studied to reach weld pool with similar size based on prior experimental results

Parameters	Room temperature	Preheated at 300 °C
Pulse energy, J	7.9	6
Peak power, kW	1.58	1.2
Power density, kW/mm^2	8	6.1

Table 1 Chemical composition of AA2024 (in wt%, bal. Al)

Aluminum alloy	Si	Fe	Cu	Mn	Mg	Cr	Zn	Ti
AA2024-O	0.16	0.30	4.30	0.61	1.45	0.05	0.08	0.05

It should be mentioned that in order to calculate SCI, crack counts were made relative to their initiation sites regardless of their length and propagation characteristics.

2.2 Simulation

Finite element modeling of heat transfer during laser welding was used to provide data some of the required model inputs such as cooling rate (dT/dt), solidification rate (r), and the temperature profile (T(x)). For the simulation, a two-dimensional axisymmetric model was developed for the solution domain as depicted in Fig. 1a. The solution domain was meshed with linear rectangular elements and mesh size independency. The elements close to the surface subjected to the heat source were more finely meshed (as illustrated in Fig. 1b), as this zone experiences steeper thermal gradients. Thermal modeling of the welding process was performed using the commercially available finite-element package ABAQUS.

Temperature-independent isotropic thermo physical properties for AA2024 were assumed in the simulations. The laser power distribution was assumed to be a uniform heat flux with a laser beam diameter at the focal point of 500 µm. Moreover, radiations and free convections were applied at all surfaces. The values of the simulation input parameters are given in Table 3. It should be mentioned that due to the effect of shielding gas flow rate, the heat transfer coefficient at the top surface of the sheet was considered to be higher than at other surfaces [18]. Regarding applying the effect of laser pulse ramp down on solidification cracking behavior of 2024 alloy, the data reported by Michaud et al. was utilized [4]. It is reported that when a

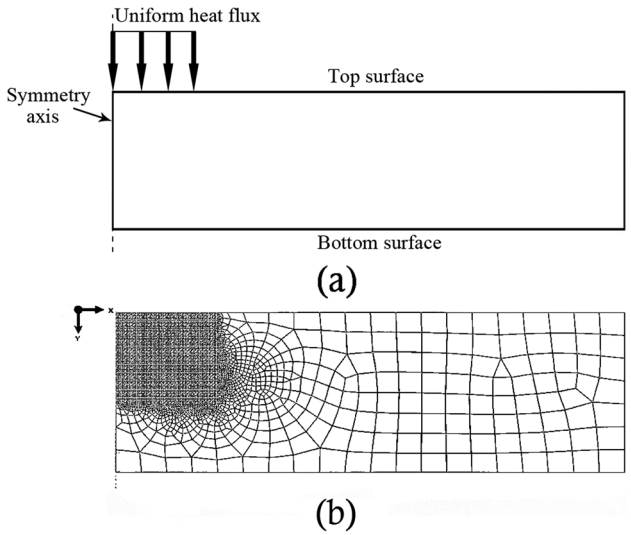

Fig. 1 **a** The solution domain and corresponding boundary conditions, **b** The meshing strategy details

Table 3 Thermo physical properties of AA2024 [18, 19]

Parameters	Value
Thermal conductivity (W.m^{-1}.K^{-1})	164
Stefan-Boltzmann constant (W.m^{-2}.K^{-4})	5.67×10^{-8}
Emissivity	0.03
Specific heat capacity of solid (J.kg^{-1}.K^{-1})	481
Specific heat capacity of liquid (J.kg^{-1}.K^{-1})	1273
Density of solid (kg^{-1}.m^{-3})	2780
Density of liquid (kg^{-1}.m^{-3})	2375
Thermal expansion coefficient ($\times10^{-6}$)	14
Heat transfer coefficient (W.m^{-2}.K^{-1})	Top surface: 20 Other surfaces: 5

specified temporal ramp-down shape is used instead of a conventional square-wave pulse, the solidification cracks were eliminated. In this condition, after radiation of the laser for 5 ms with a peak power of 1.6 kW, the laser power gradually decreased with a ramp down time of 10 ms until it reached zero after 15 ms from pulse irradiation, instead of sudden termination of the laser radiation in square-wave pulse. It should be remember that laser pulse shaping was not performed in this study and the capabilities and predictive power of the model were demonstrated using reported experimental data by Michud on pulse shaping. The governing equation of heat transfer is as follows:

$$\frac{\partial^2 T}{\partial^2 r'}+\frac{\partial^2 T}{\partial^2 y}=\frac{\rho c_p}{k}\frac{\partial T}{\partial t} \tag{1}$$

in which T is the temperature, r' is the radial distance from the center of the melt pool, y is the depth into the sheet from the top surface, t is time, k is thermal conductivity, and c_p is specific heat capacity. The boundary condition used in the simulations was:

$$k\frac{\partial T}{\partial n}-\mu.q+h(T-T_0)+\sigma'\varepsilon'(T^4-T_0^4)=0 \tag{2}$$

in which σ' is Stefan–Boltzmann constant, h is heat transfer coefficient, ε' is emissivity, and T_0 is ambient temperature, and n is vector normal to the surface. In this equation, q and μ are the surface heat flux and absorption coefficient, respectively. It should be noted that when simulation of welding with pulse shaping, the variable q was time-dependent, and for any time, step corresponding the heat flux was calculated regarding the ramp down slope. The absorption coefficient of aluminum at different base metal temperatures was previously reported [17]. The initial condition was then:

$$T\left(r',z,0\right)=T_i \tag{3}$$

in which T_i is the initial temperature of the base metal.

3 Results and discussion

3.1 Experimental results

The top view of four laser spot welds for both base metal initial temperatures studied are presented in Fig. 2. The weld pool is divided into two main regions, as seen in the microstructure of the weld metal in Fig. 2. One is the equiaxed zone, which forms in the inner part of the pool, and the other is the columnar zone, which is in the outer part of the weld pool. Because of the slower cooling rate in preheated samples, the equiaxed grain size is coarser. The cross sections of two spot welds from both welding conditions are also illustrated in Fig. 3.

Solidification cracks within the weld are indicated by black arrows in each image. By inspection of these images, the level of cracking is reduced when the base metal is pre-heated to 300 °C. The average number of crack observed in top and cross sections of each weld spot is given in Table 4.

Preheating reduces the crack numbers in both top and cross sections. Furthermore, regardless of the base metal's initial temperature, the cross sections of created samples using square-wave pulse, has less cracks than their top sections. Moreover, it was observed that in welds made on room temperature base metal, the majority of cracks start from a location near the FL where the microstructure is columnar structure, whereas the crack starts from a location closer to the weld center in preheated samples, where the dominant microstructure of initiation sites is equiaxed structure.

Figure 4 shows an SEM micrograph of a typical crack surface. The cellular morphology of the crack surface indicates that these are indeed solidification cracks that formed in the last stages of solidification.

3.2 Simulation results

Verification of the finite element simulation results was conducted by comparing the predicted weld pool profile with those obtained in the experiments; a comparison of the weld cross section from both simulation and experiment is illustrated in Fig. 5a. The Hunt model was also employed to validate the thermal results of the simulation, in which the primary dendrite spacing (λ_1) was related to G and r as follows [4]:

$$\lambda_1 = C \times G^{-0.5} \times r^{-0.25} \tag{4}$$

in which $C = 2.0573 \times 10^{-2}$ $K^{-0.75}cm^{0.5}$ $s^{-0.25}$ [4]. The value of λ_1 for both base metal temperatures as predicted using the Hunt model (Eq. 4), with the predicted values of G and $\dot{T}$ from the FE simulation as model inputs, and the results are reported in Table 5. Based on SEM images as shown in Fig. 5b, the primary dendrite arm spacing was measured in some grains near FL for the samples welded with and without base metal preheating, and the average value of λ_1 for each condition is presented in Table 5. From the table, it can be seen that there is reasonable agreement between the predicted and measured values, which confirms that the reasonable accuracy of the FE simulations. Moreover, there is good agreement between the simulation results obtained in this study (e.g., cooling rate) and those reported in the literature [4, 16, 17].

4 Discussion

4.1 Cracking model

To predict the distribution of solidification crack initiation locations along the weld pool radius, a new approach will be developed in this section. This approach is adapted from the cracking model proposed by Sheikhi et al. [17], which accounts for the competition between the volume change rate and liquid feeding rate during the terminal stages of solidification.

As temperature decreases during solidification, the crack susceptibility begins to increase when solid grains begin to impinge on one another at a point referred to as the coherency temperature (T_{coh}). As the temperature continues to decrease and solid phase fraction (f_s) increases, the permeability decreases and distances from coherency point (l) increases. Both of these factors reduce the liquid flow rate toward the roots of solid cells in accordance with Darcy's law [14]. Moreover, thermally induced strains increase as temperature decreases, due to differences in the levels of shrinkage and thermal contraction throughout the melt pool and base metal. Subsequently, the crack susceptibility continues to increase up to a point referred to as the bridging temperature (T_{brid}), below which the number of bridge between grains begins to rise and network of solid grains is sufficiently connected such that is can sustain mechanical deformation and the crack susceptibility decreases again. Thus, for any location in the solidifying weld pool, the most susceptible temperature to cracking is just temperature of bridging. According to Sheikhi's criterion [17], solidification cracks will form when the rate of liquid backfilling becomes less than the rate of volume shrinkage between coherency and bridging points, herein referred to as the vulnerable zone.

It is deduced from the model proposed by Sheikhi et al. [17] that for a given vulnerable zone length (physical distance in the melt pool between coherency and bridging points), and solidification rate which are denoted as l and r, respectively, the boundary condition for crack initiation can be determined by:

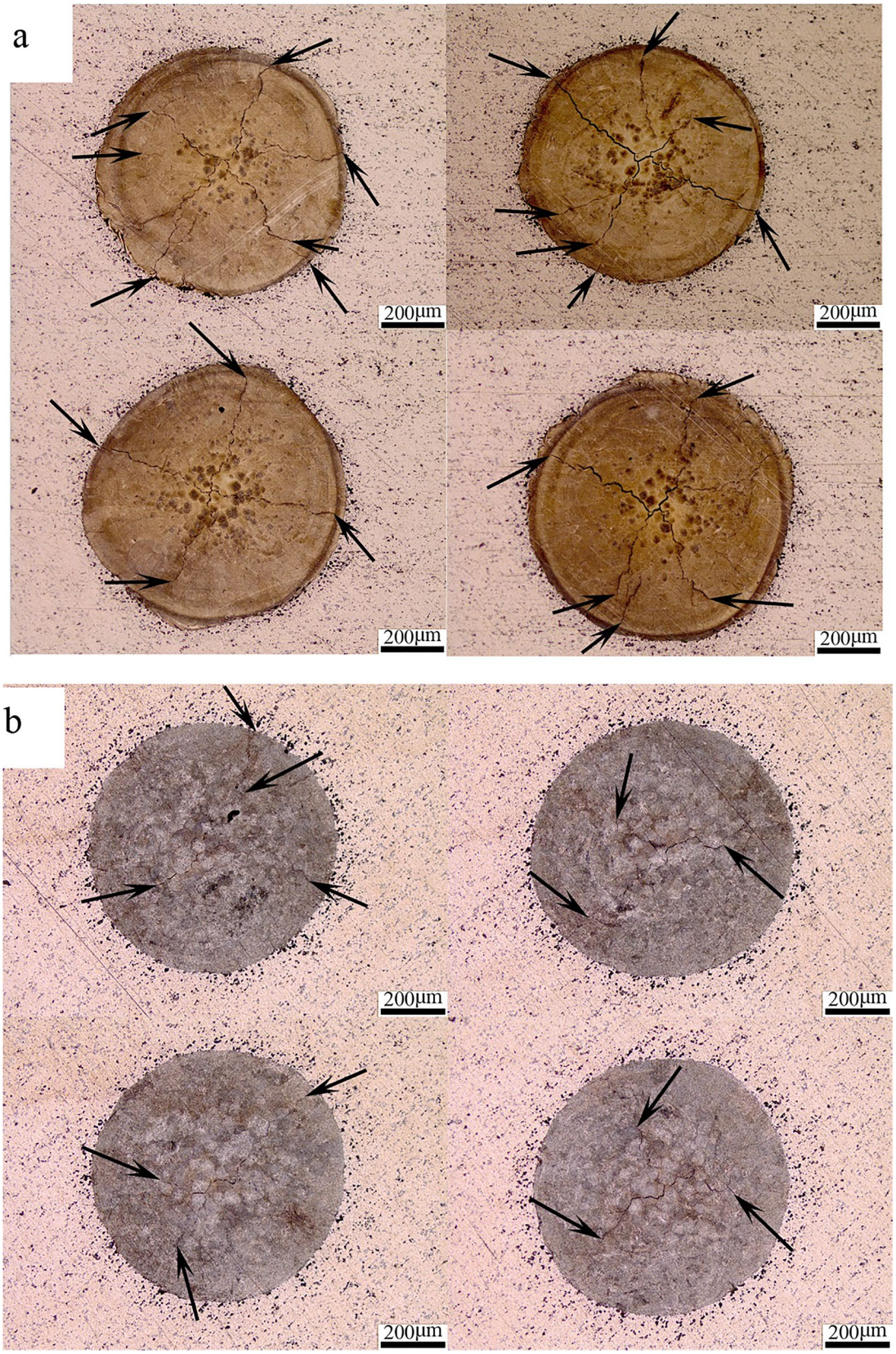

Fig. 2 Top view of four individual laser spot weld samples created using square-wave pulse shape and an initial base metal temperature of **a** room temperature, **b** 300 °C. The black arrows indicate the crack initiation sites in the weld pool

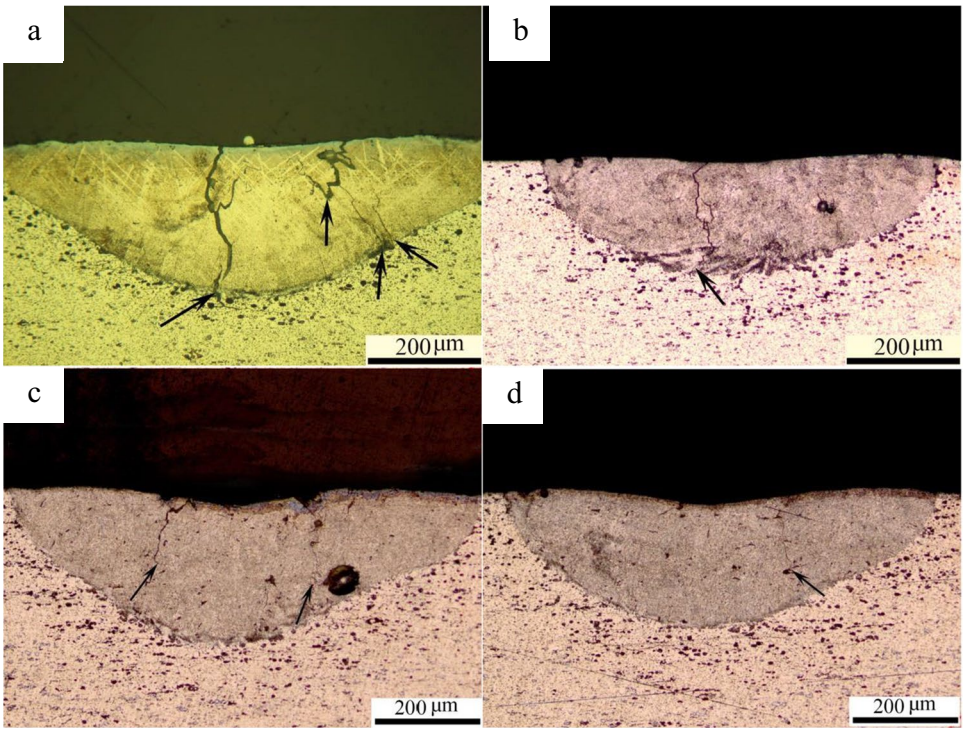

Fig. 3 The cross-section microstructures of two laser spot welds created using a square-wave pulse shape and an initial base metal temperature of **a** and **b** room temperature, **c** and **d** 300 °C. The black arrows indicate the crack initiation location in the weld pool

Table 4 The average crack number observed in top and cross sections of weld spots

Base metal initial temperature	Cross section	Top section
Without preheating (room temperature)	4 ± 2	6 ± 2
Preheated at 300 °C	2 ± 1	3 ± 1

$$r \times l = \varphi \tag{5}$$

where

$$\varphi = \frac{f_l^2 {\lambda_1}^2 \Delta P}{(180\pi\eta\Delta T)\left(1-f_l\right)^2\left(\frac{\beta_{Sh}}{1+\beta_{Sh}\left(1-f_l\right)}\cdot\frac{1}{(1-k)\left(m_l C_0\right)}\left(f_l\right)^{2-k}+\beta_{th}\right)} \tag{6}$$

in which f_l is the liquid volume fraction in the vulnerable zone, λ_1 is the primary dendrite arm spacing, $_k$ is the equilibrium solute distribution coefficient, m_l is the slope of the liquidus, η is the liquid phase viscosity, and β_{th} is the coefficient of thermal expansion. Also β_{sh} represent the shrinkage factor and $\beta_{Sh} = \frac{\rho_s}{\rho_l} - 1\left(\beta_{Sh} > 0\right)$ where ρ_s and ρ_s are solid and liquid densities, respectively. ΔT is the vulnerable temperature range, and ΔP is the pressure difference between bridging and coherency points. It was indicated in previous studies [20, 21] that based on the rheological behavior of semisolids, it is reasonable to assume that ΔP is equal to the stress obtained from following equation:

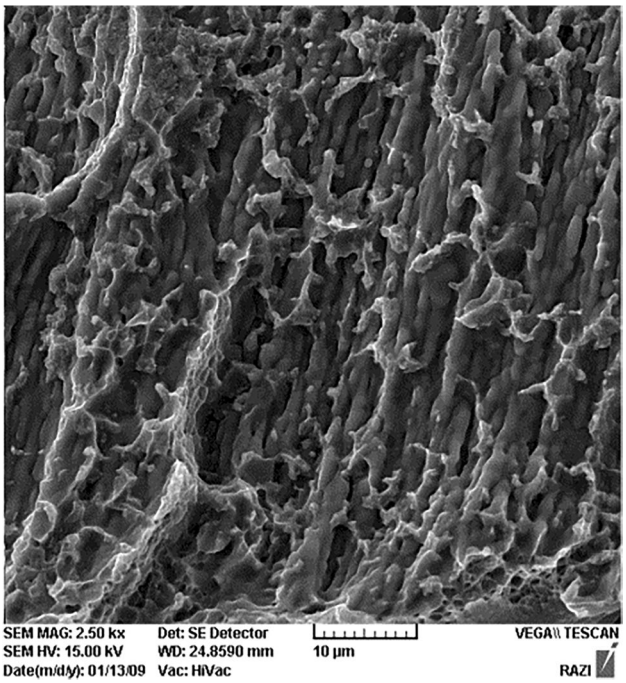

Fig. 4 An SEM micrograph of cellular crack surface in a weld pool created without preheating

$$\sigma = \sigma_0 \exp\left(\alpha f_s\right).\exp\left(\frac{mQ}{\Re T}\right)(\dot{\varepsilon})^m \tag{7}$$

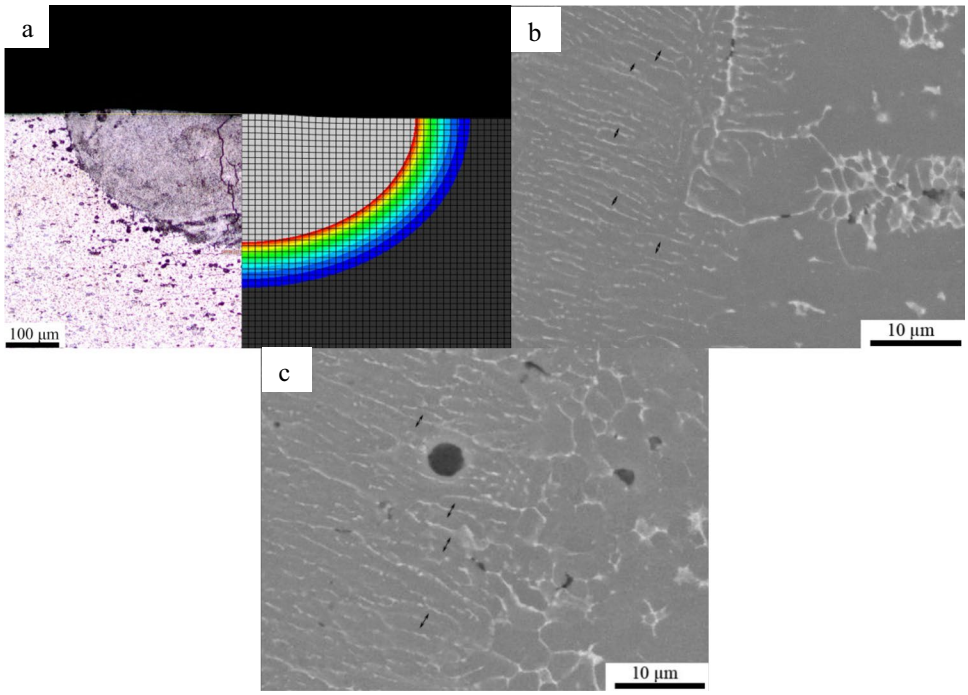

Fig. 5 **a** Comparison of experimental and FE simulated melt pool shape for a sample welded without base metal preheating. **b** λ_1 near FL in a weld pool created without base metal preheating, **c** λ_1 near FL in a weld pool created with base metal preheating

Table 5 Comparison of the measured predicted and measured primary dendrite arm spacing near the FL

Base metal initial temperature	G – finite element (K/cm)	r – finite element (cm/s)	λ_1 – Hunt equation (µm)	λ_1 – measured (µm)
Room temperature	3850	29	1.43	1.9 ± 0.5
300 °C	2270	12	2.32	2.5 ± 0.5

where T is the bridging temperature in Kelvin, f_s is solid fraction, Q is the activation energy, $\dot{\varepsilon}$ and m are strain rate and strain rate sensitivity coefficient, respectively, α and σ_0 are material constants, and $\Re$ is the gas constant. These parameters were reported for an Al-Cu alloy as $\sigma_0 = 4.5$ Pa, $m = 0.26$, $\alpha = 10.2$, and $Q = 160$ kJ.mol^{-1} [11, 20].

M'hamdi et al. [18] estimated the maximum linear strain rate experienced by the vulnerable zone at the line of symmetry in the weld pool using the following equation:

$$\dot{\varepsilon} = \frac{1}{3}\psi(f_s)\beta_{th}.\left(\frac{dT}{dt}\right) \tag{8}$$

where $\psi(f_s)$ is a solid-fraction dependent function which describe the effect of solid fraction on strain rate and it changes between 0 to 1, i.e., from 1 for $f_{s,brid}$ and zero for solid fraction over $f_{s,coh}$.

ΔT in Eq. (6) corresponds to the vulnerable temperature range, i.e., the temperature range that cracking may occur, and it can be obtained as follows:

$$\begin{cases} \Delta T = T_{coh} - T_{\text{brid}} & f_{l,\text{brid}} > f_E \\ \Delta T = T_{coh} - T_E & f_{l,\text{brid}} \le f_E \end{cases} \tag{9}$$

where T_E and f_E are eutectic temperature and eutectic fraction, respectively, and $f_{s,brid}$ and $f_{s,coh}$ are solid fractions corresponding to bridging and coherency temperatures, respectively. To determine the upper and lower boundaries of vulnerable zone, i.e., $f_{s,brid}$ and $f_{s,coh}$, and their corresponding temperatures, the following approach was proposed by Sheikhi et al. [17]. Based on this model, a solidification cracking susceptibility (SCS) can be related to the vulnerable temperature range (ΔT) by [17]:

$$\text{SCS} = \Delta T^2 \tag{10}$$

However, Eq. (10) only indicates the probability of cracking and was proposed as an index for ranking the alloys with regards to their relative sensitivity under similar solidification regimes, i.e., similar r and G. In other words, SCS is a comparative quantity and can be assessed by crack density only if the welding or casting conditions are fixed. Therefore, the coherency and bridging temperatures can be calculated in such a way that the best agreement between ΔT^2 and experimentally determined composition-dependent cracking susceptibility curves is obtained. The accuracy of Eq. (10) in the prediction of the Λ-shaped cracking susceptibility curve for Al-Cu and Al–Mg binary aluminum alloys were investigated in previous investigations and showed good agreement between the calculated cracking susceptibility with experimental measurements [16, 17]. For prediction

of actual solidification crack formation, another parameter (SCI) was proposed by Sheikhi et al. [17] which can be obtained as follows:

$$\mathrm{SCI} = \frac{r \times l - \varphi}{\varphi} \tag{11}$$

According to this index, a crack will occur only if SCI > 0 (i.e., $r \times l \geq \varphi$), and crack severity has a direct and inverse relationships with $r \times l$ and φ, respectively.

The vulnerable temperature range (ΔT in Eq. (9)) is mainly affected by the solute distribution coefficient at the solid/liquid interface (k) [16]. Due to the high r in pulsed laser welding, k deviates from the equilibrium value. To consider this effect, the resultant undercooling as a result of rapid solidification ($\Delta T'$), the r-dependent partition coefficient (k_r) at the solid/liquid interface should be applied to the Scheil model.

The total under cooling (ΔT_t) is equal to the summation of constitutional under cooling (ΔT_c), thermal undercooling (ΔT_{th}), curvature undercooling (ΔT_g), and kinetic undercooling (ΔT_k). However, as reported by J-Aziz et al. [19] and Katayama et al. [22], the amount of ΔT_g, ΔT_k and ΔT_{th} are very small and so can be ignored in rapid solidification of Al alloys. Katayama et al. [22] also demonstrated that, in rapid solidification, constitutional undercooling has a major role in the total undercooling. So:

$$\Delta T_t \approx \Delta T_c = \left(m_r C_L^*\right) - \left(m_0 C_0\right) \tag{12}$$

where C_0 is the initial liquid composition, C_L^* is the composition of liquid at the dendrite/cell tip, m_0 is the equilibrium liquidus slope, and m_r is the r dependent liquidus slope. More explanation about C_L^* and m_r are given in Appendix A.

Scheil's equation was established based on the assumption of local equilibrium element partitioning at the solid/liquid interface, and must be modified for non-equilibrium condition at the solid/liquid interface induced by rapid solidification rates. Rapid solidification is typically defined as solidification that occurs faster than 0.01 m/s. Based upon Scheil's equation, the solidification path (f_s-T curve) can then be calculated as follows:

$$T = T_m - m_0 C_0 \left(1 - f_s\right)^{k_0 - 1} \tag{13}$$

So, for rapid solidification T should be replaced by T' as follows:

$$T' = T - \Delta T_t \approx T - \left(m_v C_l^* - m_0 C_0\right) \tag{14}$$

Considering the effect of r at the dendrite/cell tip, the curve of f_s versus temperature is shifted to lower temperature for the same solid fraction, i.e., from T in Scheil's equation to T'. Furthermore, when r increases, not only does the solidification temperature (T) decrease to T', but the equilibrium eutectic temperature, T_E, also decreases to T_E'.

$$T_E' = T_E - \Delta T_E \tag{15}$$

where ΔT_E can be computed using TMK model, proposed by Trivedi et al. [23], see Appendix B. The TMK model showed that the parameters of ΔT_E at high solidification rates are dependent on r. With regards to these temperature reductions, it is concluded that the f_s-T curve shifts to lower temperatures as a result of rapid solidification. The physical properties of Al-Cu alloys and the parameters required to calculate T' and T_E' are given in Table 5 in Appendix C [24].

Hence, the vulnerable temperature range ($\Delta T'$) in line with Eq. (9) can be rewritten as a function of new eutectic fraction under rapid solidification condition (f_E') as follows:

$$\Delta T' = \begin{cases} T'_{coh} - T'_{brid} & f_{l,brid} > f'_E \\ T'_{coh} - T'_E & f_{l,brid} \leq f'_E \end{cases} \tag{16}$$

Regarding the above discussions, the factors affecting crack initiation and, in turn SCI, can be summarized as is depicted in Fig. 6.

It should be noted that SCS only accounts for material properties, and therefore can only provide a qualitative/relative assessment and a numbers of alloys can be ranked by this index from a cracking chance viewpoint when they experience similar solidification conditions, whereas SCI accounts for both material properties and the process conditions and, therefore, predicts the actual cracking susceptibility.

4.2 The effect of rapid solidification on T vs. f_s curve and vulnerable temperature range

The effect of r on the solidification path is shown in Fig. 7a for a binary Al-4.5wt.%Cu alloy. This figure shows that as the solidification rate increases, the f_s-T curve shifts to lower temperatures and the eutectic fraction decreases. It was previously demonstrated that in pulsed laser welding of Al-Cu alloys, $f_{s,coh}$ and $f_{s,brid}$ do not change as a result of rapid solidification (for r lower than 1 m/s) and that $f_{s,coh} = 0.9$ and $f_{s,brid} = 0.98$ [17]. Figure 7a shows that for Al-4.5% Cu alloy, the vulnerable temperature range dramatically increases when equilibrium at solid/liquid interface in Scheil condition was changed to non-equilibrium condition of 0.5 m/s. Similar computations were performed for different solidification rates and the results are depicted by red data points in Fig. 7b.

The solid black curve in Fig. 7b is the best exponential fit to the data points to find a relation between $\Delta T'$ and

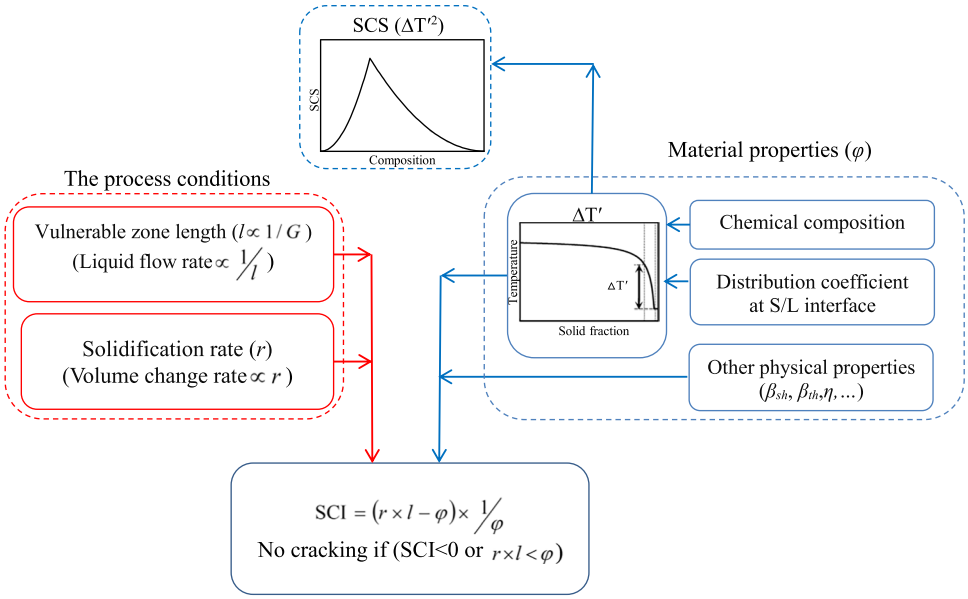

Fig. 6 Diagram showing the relation between factors governing solidification cracking based on the model studied in the present investigation. SCS can be used as an index for ranking the alloys with regard to their susceptibly to solidification cracking based purely on the material properties, but SCI predicts the occurrence of cracking by accounting for both material properties and process conditions

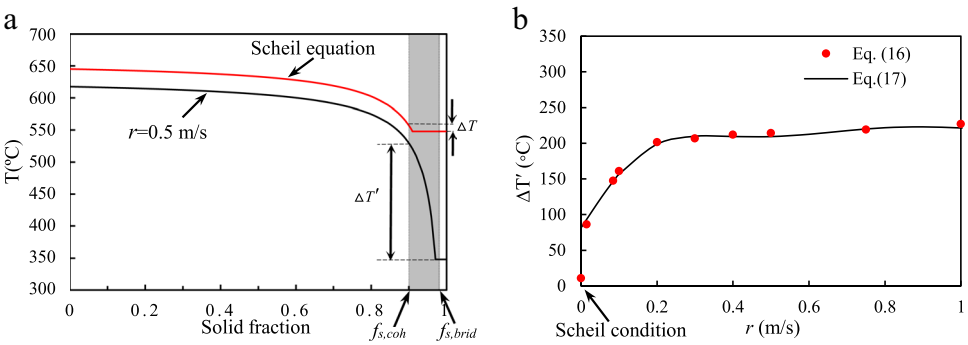

Fig. 7 The effect of the solidification rate on **a** the solidification path (f_s *vs.* T curve) for $r = 0.5$ m/s and **b** the vulnerable temperature range ($\Delta T'$) as a function of solidification rate for a Al-4.5% Cu alloy

solidification rate. This curve was plotted by the following equation. The corresponding equation is:

$$\Delta T' = \exp\left(-7.6r^6 + 38.4r^5 - 76.2r^4 + 75.2r^3 - 38.5r^2 + 9.7r + 4.4\right) \quad (17)$$

where r is in m/s. It should be note that this equation is credible only for solidification rate ranges between 0 and 1 m/s.

4.3 The effect of process condition on solidification characteristic

In this section, the effect of base metal pre-heating and pulse shaping on the solidification characteristics most relevant to solidification cracking and SCI will be investigated. For steady state processes, the conditions at the bridging point (i.e., corresponding r and l) are fixed during the process. But for unsteady-state processes, including pulsed laser welding process, the bridging point at different locations in weld pool experiences different r and l during solidification. As solidification progresses, the bridging point moves toward the surface of the weld pool and the corresponding solidification conditions (i.e., r, l, and φ) experience some changes. The above-mentioned parameters for each specific point in the fusion zone must be calculated at the time when that location is at its peak level of cracking susceptibility (i.e., $T = T_{brid}$). In this regard, the values of r and l at T_{brid} were computed for different points along the weld pool radius.

For all of the welding conditions in this study, the variations of l, r and $\dot{T}\left({}^{dT}/_{dt}\right)$ were calculated using FE method simulation along the symmetric lines of the weld pool in the top section (Fig. 8a) and transverse cross section (Fig. 8b).

The results of FE analysis show that for the studied welding conditions (square-wave and ramp down pulse shape), the variations of l, r, and $\dot{T}$ as a function normalized weld pool dimension in the transverse cross and top sections follow the same pattern as depicted in Fig. 8c for l, r as example. Considering this similarity, the following discussions include the analysis obtained from the transverse cross section only (along symmetric line). The variations of r, $\Delta T'$,

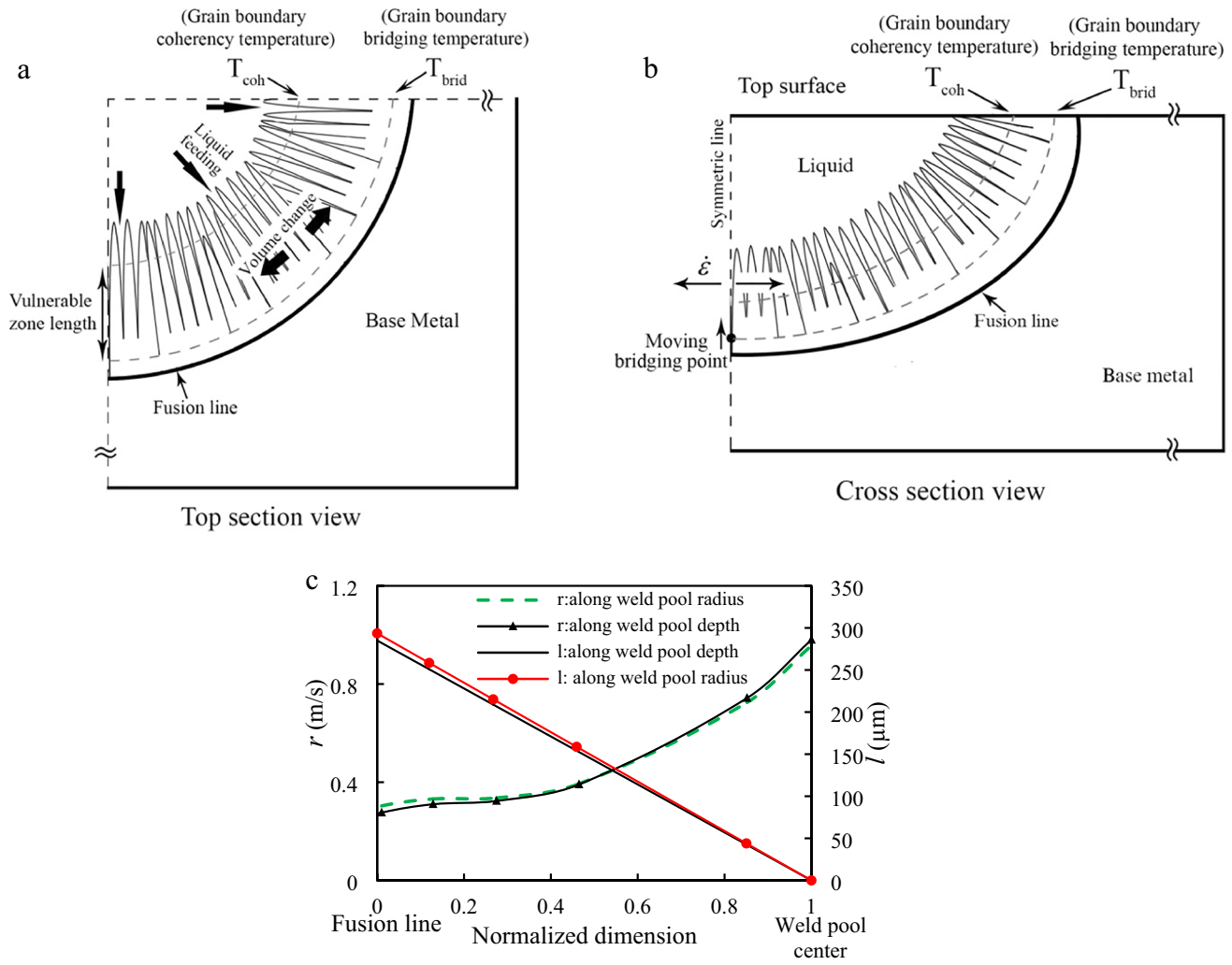

Fig. 8 Factors influencing cracking along weld pool depth and weld pool radius. Schematic illustrations of governing factors in a solidifying single laser spot weld pool from **a** top section view and **b** transverse cross section view. **c** Comparison of the variations of r and l at bridging temperature along depth and radius of weld pool created without base metal preheating

l, and $\dot{T}$ along the weld pool radius are shown in Fig. 9. In these figures, "0" and "1" represent FL and weld pool center, respectively. The variations of l along the weld pool radius are shown in Fig. 9a. This figure shows that l versus radius is linear when the laser pulse shape was square-wave, but l is always greater when the substrate is preheated. The use of pulse shaping is predicted to results in a deviation from the linear trend; a nearly constant l value is observed up to approximately radius = 0.5, after which is follows the same trend and magnitude as the square-wave pulse. Moreover, it is seen that reasonably the longest l occurs in the preheated sample, since G decreases as a result of preheating process.

With moving the solidus isotherm away from fusion boundary toward weld pool center, the solidification rate (r) and, in turn, $\Delta T'$ were found to continuously increase in all conditions. It should be mentioned that $\Delta T'$ in Fig. 9c was calculated based on Eq. (17) and given solidification rate in Fig. 9b. The significant decrease in both of solidification rate and $\Delta T'$ as a result of pulse shaping compared to a square-wave pulse is obvious in Fig. 9b and c.

The cooling rates that correspond to the bridging point as it moves along the weld pool radius for different conditions are shown in Fig. 9d. It can be seen that the cooling rate is predicted to increase as the bridging point approaches the top of the weld pool for all cases. It is interesting to note that cooling rate in the first half of weld pool as a result of pulse shaping was close to preheated sample. Furthermore, it can be seen that cooling rate of preheated weld is lower than for other welding conditions in most portion of weld pool radius, and that the cooling rate in the pulse shaping condition approaches the cooling rate of the non-preheated condition towards the weld pool center.

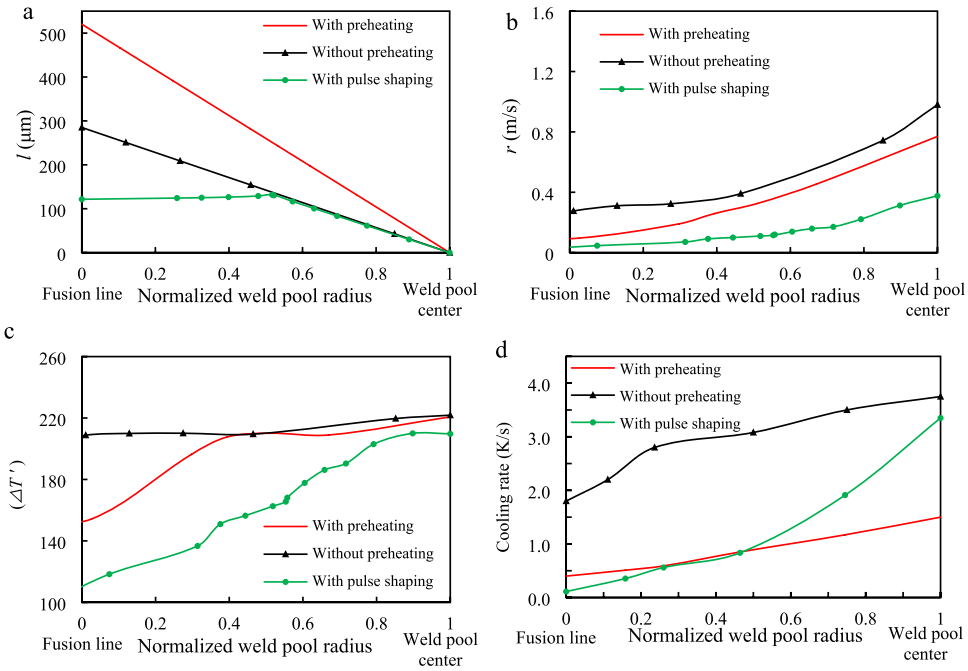

Fig. 9 Variation of parameters affecting SCI versus normalized melt zone radius. **a** Vulnerable zone length, **b** solidification rate, **c** vulnerable temperature range, **d** cooling rate

4.4 Interpretation

Figure 10 shows the variations of φ and $r\times l$ along weld pool radius. It should be mentioned that to consider the effect of rapid solidification on φ, the parameters of $\Delta T'$, k_r, and m_r were used instead ΔT, k and m_l in Eq. (6), respectively. To calculate the variations of φ within the weld pool created under different welding conditions (i.e., base metal pre-heating and pulse shaping), the variations of l, $\Delta T'$, and ΔP along weld pool were considered. ΔP was related to the calculated cooling rate in Fig. 9d by Eqs. (7) and (8). Moreover, the primary dendrite arm spacing was calculated using Eq. (4). Figure 10 shows that for most of the weld pool created by square-wave pulse $r\times l$ is larger than φ and ramp down pulse shaping increases φ and the largest φ belongs to this condition. In the cases that a square-wave pulse was employed for welding, pre-heating the base metal results in an increase in φ (Fig. 9a and b). It should be mentioned that $\Delta T'$, m_r, and k_r all increase with moving from the FL to the weld pool center, and all of these parameters act to decrease φ.

Moreover, for weld pools created with square-wave pulses, it can be seen that the maximum $r\times l$ occurs at the FL for no preheating, but between 0.4 and 0.6 for welds created with a pre-heat. Conversely, for the welds made with pulse shaping (Fig. 10c), it can be seen that $r\times l$ increases by moving from FL to weld pool surface, since in the first half of weld pool l is constant and r increases (Fig. 9a and b), but after reaching a maximum value at around half way to the weld surface $r\times l$ begins to decrease due to a reduction in l (Fig. 9b).

The calculated SCI for different welding conditions are illustrated in Fig. 11. Based upon Eq. (11), cracking occurs when $r\times l > \varphi$ (i.e., SCI > 0). Therefore, among all welding conditions studied here, the required condition for crack prevention throughout the entire weld pool is only provided for welds performed using pulse shaping condition because along the entire weld pool radius $r\times l < \varphi$ as illustrated in Fig. 10c, and therefore, there is no curve representing the pulse shaping condition in Fig. 11.

Figure 10 shows that in the cases when a square-wave pulse is employed, the $r\times l$ curve is greater than φ throughout most of the weld pool radius, and then falls below φ toward the top of the weld pool. Consequently, Fig. 11 indicates that for welds created with a square-wave pulse, SCI > 0 throughout most of the weld pool for both base metal initial temperatures, indicating that cracks are expected to be initiated. It can also be seen that unlike the non-preheated sample, in which SCI continuously decreases with increasing height through the melt pool, SCI has a non-monotonic behavior with respect to weld pool radius in the sample with base plate pre-heating, with the maximum SCI predicted to be between a normalized radius of 0.4 to 0.6. It is important to note that while new crack initiation is unlikely to occur close to the weld pool center (SCI < 0), early crack initiation in the area where SCI > 0 can propagate to the center.

The percent of cracks initiated between x_1 and x_2 through the weld pool radius can be obtained by dividing the area under the SCI curve at corresponding distance by the total area under the SCI curve between the FL (0) and the weld pool center (1) as follows:

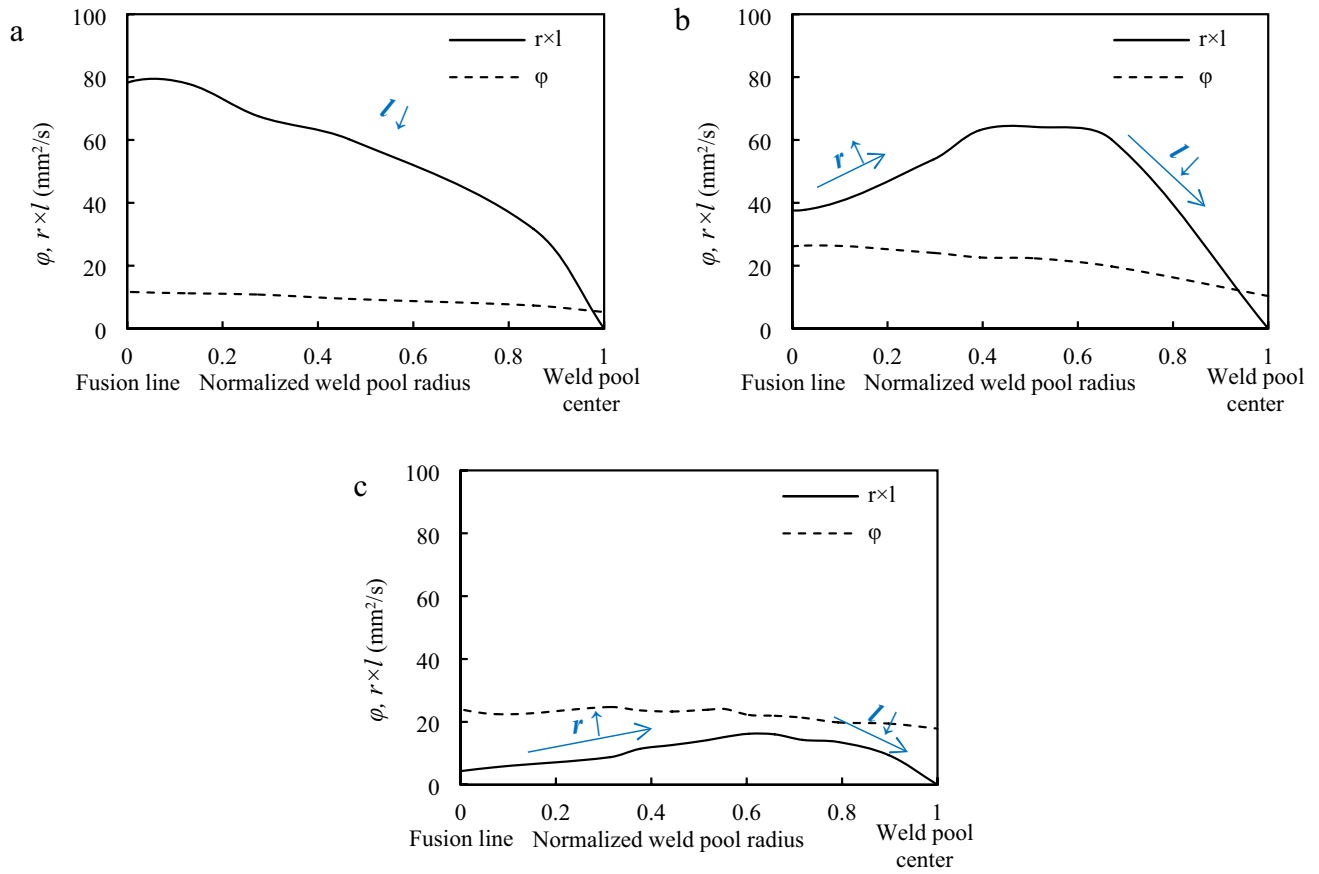

Fig. 10 The variations of $r \times l$ and φ versus normalized weld pool radius corresponding to various welding conditions **a** without preheating, **b** with 300 °C preheating, and **c** with pulse shaping

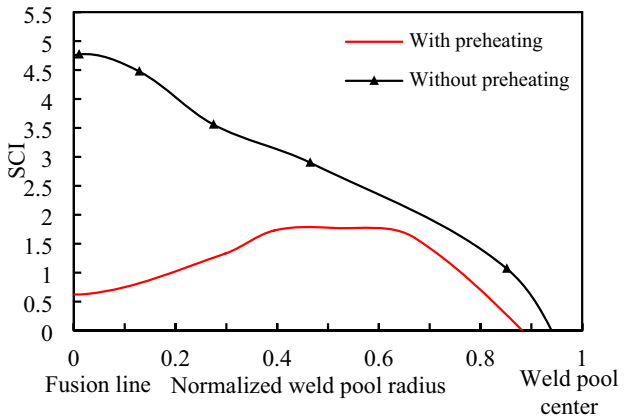

Fig. 11 Variations of solidification cracking indexes against the normalized weld pool radius for different welding conditions. For the melt pools created with pulse shaping, SCI < 0 for all x and required conditions for cracking were not met

$$\text{The percent of intiated cracks atdistance of } x_1 - x_2 = \frac{\int_{x_1}^{x_2} SCI.dx}{\int_{0}^{1} SCI.dx} \times 100 \tag{18}$$

In Fig. 12, the percentage of cracks as a function of corresponding initiation sites measured from both top and cross section are compared with results calculated from Fig. 11 and Eq. (20). From the figure, it can be seen that that more than 54% of solidification cracks were next to the FL in the samples without base plate pre-heating, but that decreased to about 5% with preheating. Instead, the highest proportion of crack initiation sites shifted towards the center of the weld pool when pre-heating was used. It can also be seen that although the quantitative value of cracking was not predicted very well in some cases, but it is interesting to note that, the model is excellent at predicting the trend change in crack initiation sites across the entire weld pool. In no preheated samples, it accurately predicts a monotonic

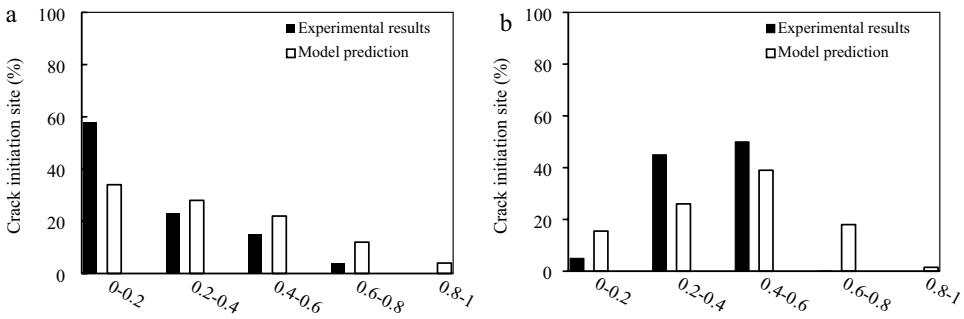

Fig. 12 Comparison of measured and predicted distribution of crack initiation sites throughout the weld pool ("0" and "1" indicate FL and weld pool center, respectively). **a** Nonpreheated sample and **b** 300 °C preheated sample

decrease and in preheated sample, it correctly predicts a nonlinear variation, i.e., increasing and then decreasing cracking index. The discrepancy in the specific value for crack initiation sites could be due to a wide number of factors (e.g., accuracy of thermo physical material properties).

For welded samples created using a square-wave pulse with and without preheating conditions, although r and l followed the same trends (Fig. 9a and b), $r \times l$ behaved differently (Fig. 10a and b). Finding the reason for this difference is critical and can help to better understand the solidification cracking phenomenon observed in Figs. 2 and 3. For this purpose, the following general equations were written for r and l as a function of normalized weld pool radius (x), assuming they are linear.

$$l \times r = -\underbrace{a(x-1)}_{l} \times \underbrace{b\left(x+b_0\right)}_{r} \tag{19}$$

where a and b are the slope of l vs. x and r vs. x curves, respectively ($0 < x < 1$ is the normalized radius through the weld pool). $b \times b_0$ is the bridging point solidification rate at the FL (i.e., $x = 0$). Representative curves of r, l, and $r \times l$ as well as corresponding parameters are shown in Fig. 13a. As $r \times l$ is significant in determining the crack initiation site distribution in the weld pool, the parameter of $x_{\max}$, is defined that it is the radius at which $r \times l$ is maximum (i.e., $\frac{d(l \times r)}{dx}\Big|_{x=x_{\max}} = 0$). Therefore:

$$x_{\max} = \frac{\left(1-b_0\right)}{2} \tag{20}$$

It is interesting to note that based on this result, $x_{\max}$ only depends on solidification rate distribution in the weld pool. Other parameters such as l do not change $x_{\max}$, but its effect on $(r \times l)_{\max}$ is obvious as depicted in Fig. 13a. As b_0 decreases, $x_{\max}$ increases, meaning that a larger fraction of cracks begin from locations closer to weld pool center. In other words, the most susceptible location to crack initiation depends only on r, but the distribution and severity of crack initiation (SCI) depends on both r and l.

According to the Fig. 13a, it can be seen that by decreasing b_0, the solidification rate decreases in all parts of the weld pool correspondingly. Based on the above assumption, i.e., a linear variation of solidification rate throughout the weld pool, b_0 can be related to the solidification rate at fusion line (r_{FL}), and solidification rate at weld pool center (r_{WC}) by:

$$b_0 = \frac{r_{FL}}{b} = \frac{r_{FL}}{r_{WC} - r_{FL}} \tag{21}$$

Combining of Eq. (20) with Eq. (19) yields:

$$x_{\max} = \frac{1}{2}\left(1 - \frac{r_{FL}}{r_{WC} - r_{FL}}\right) \tag{22}$$

Therefore, $x_{\max}$ moves towards the weld center if r_{FL} decreases or the slope of solidification rate curve increases. This slope is equal to the difference between r_{WC} and r_{FL} if the solidification rate curve is linear. In Fig. 13b, a map was plotted for $x_{\max}$ as a function of r_{FL} and$r_{WC} - r_{FL}$. Since the solidification rate increases as time proceeds after termination of laser irradiation in pulsed laser welding, Fig. 13b was plotted only for $y \geq 0$ axis, which in this region$r_{WC} \geq r_{FL}$. In the yellow shaded region, mathematically $x_{\max} \leq 0$, and it is shifted outside of the melt pool, which physically means that $r \times l$ is maximum at the FL ($x_{\max} = 0$). This figure shows that as r_{FL} decreases, the extent of the shaded zone decreases, therefore for a greater value of r_{WC}, $x_{\max}$ moves away from the FL. In Fig. 13c, $x_{\max}$ was determined as a function of the relative solidification rate enhancement from FL toward weld center line. It is seen that as r_{WC} increases in relation to r_{FL}, $x_{\max}$ is seen to migrate toward the weld center. The position of the three studied welding conditions is also specified in this figure according to the corresponding r_{WC} and r_{FL} of each condition. In line with Fig. 10, it can be seen that preheating and pulse shaping increase $x_{\max}$ (i.e., shift crack initiation sites away from the FL). Some of the differences between predicted $x_{\max}$ in Figs. 10 and 13b and c are due to the fact that in Fig. 13, $x_{\max}$ is calculated based on the assumption of a linear distribution of the solidification rate in the weld pool, while as seen in Fig. 10, there is a slight deviation from the linear state.

The effects of r on $r \times l$, φ, and SCI are shown in the Fig. 14a. In this figure, it was assumed that b was the same for both r_1 and r_2 and $r_1 = 3\ r_2$. Also, l was kept constant for both

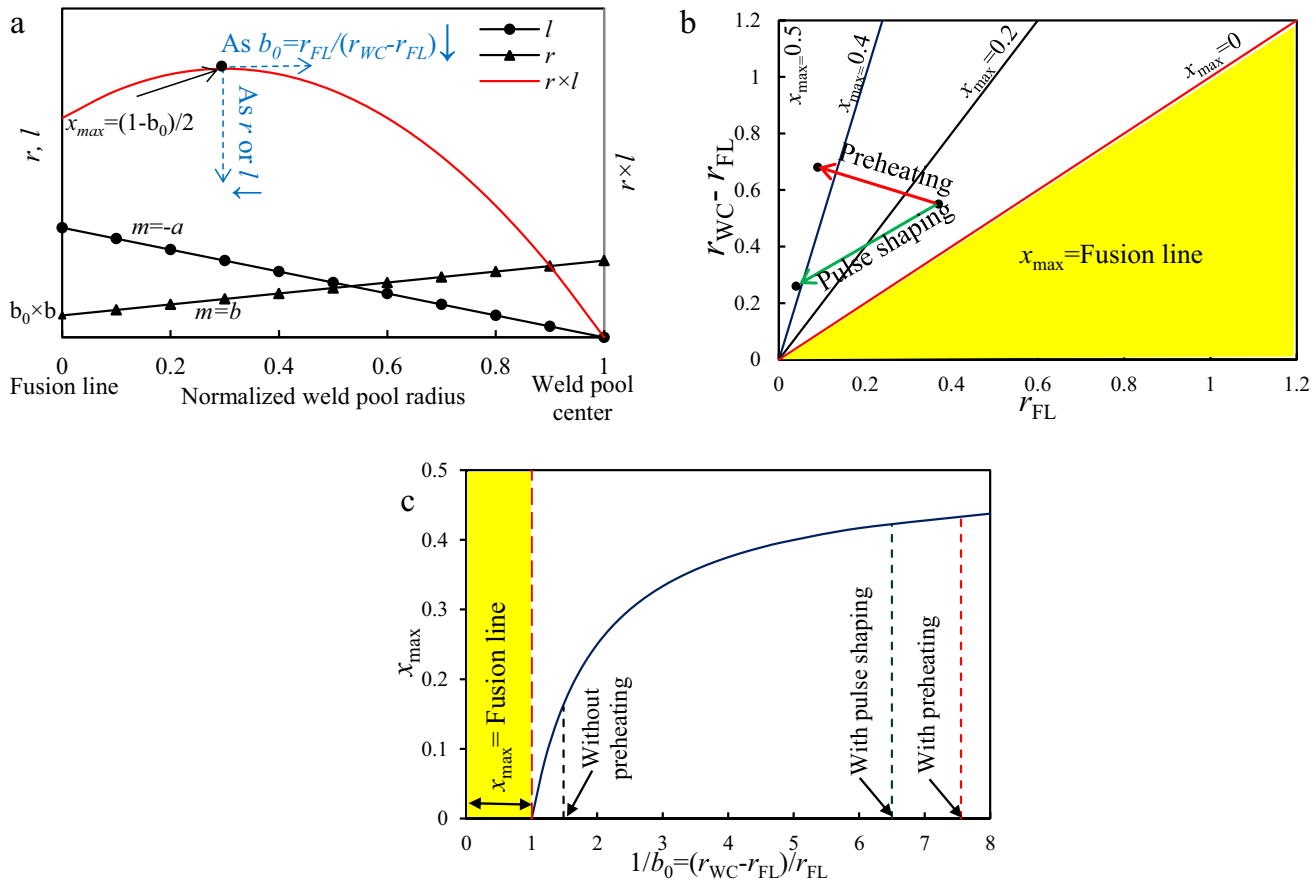

Fig. 13 The typical variations of $r \times l$ versus normalized weld pool radius. **a** The effect of r and l curves on $r \times l$, **b** the position of x_{max} in the weld pool as a function of solidification rate at fusion line (r_{FL}) and weld pool center (r_{WC}), and **c** x_{max} versus the relative solidification rate enhancement from FL toward weld center line. The situations corresponding to any welding condition are also specified on the b and c

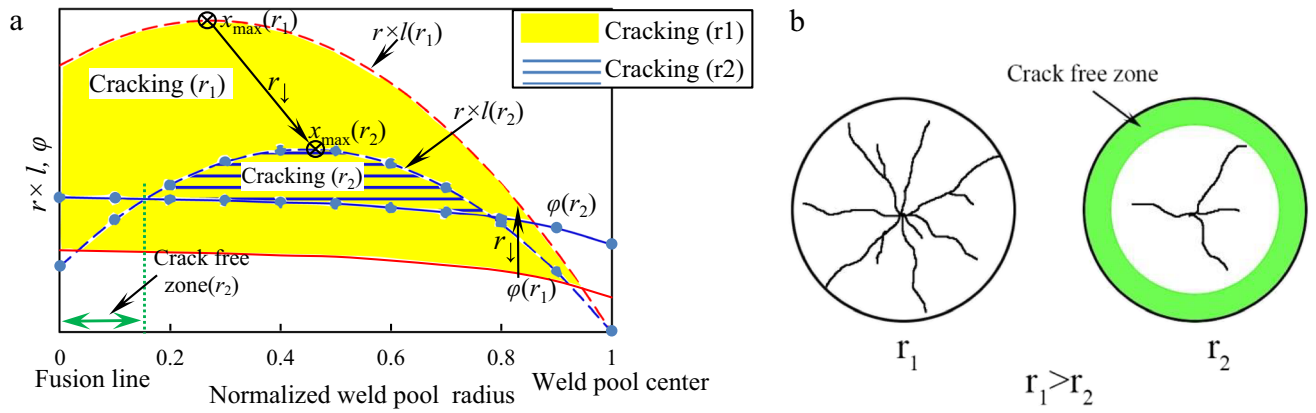

Fig. 14 The effect of solidification rate (r) on cracking. **a** The effect of r reduction on x_{max} and SCI and distribution of crack initiation sites. **b** The schematic illustration of predicted cracking behavior in spot laser weld at two different solidification rates of r_1 and r_2 based on part "a". Solidification rate reduction was applied only by reduction of b_0, while b and l were kept constant ($r_{FL,1} = 3r_{FL,2}$ and $b_1 = b_2$)

cases. It can be seen that the $r \times l$ curve shifts downward and to the right, as explained in Fig. 13a. It should be noted that φ increased as a result of a reduction in r, due to increasing m_r, k_r, and decreasing λ_1. Consequently, as shown in Fig. 14a, a decrease in r leads to a decrease between $r \times l$ and φ curves. Therefore SCI will decreases as a first result of r reduction. Moreover crack initiation site moves away FL, and a crack free zone will be formed near the FL (where $\varphi > r \times l$ and SCI > 0) as a second result. Both of these results are shown schematically in Fig. 14b. It should be mentioned that SCI describes crack initiation, so no cracks will be present for $x < \sim 0.2$ for r_2, and no cracks will initiate past $x \sim 0.8$, but existing cracks between 0.2 and 0.8 could propagate into the center.

It is important to note that the above conclusion is also consistent with the experimental results that have been frequently reported in independent studies where non-optimized down-ramp pulse shaping was used for welding [25–27]. In such condition, where the cracks are reduced but not removed, it was found that most of the cracks start from places close to the center of the weld pool as the slope of ramp down decreases.

5 Conclusions

In this study, a material- and process-dependent model was used to accurately predict the distribution of cracks in a pulsed laser weld pool of aluminum alloy AA2024. The model was able to account for different process conditions (base metal pre-heating and laser pulse shaping) and non-equilibrium solidification conditions. Based on this model, the variation of two main factors throughout the weld pool were investigated to predict the distribution of crack initiation site: $r \times l$ (process dependent factor) and φ (material dependent factor), where cracking occurs if $\varphi > r \times l$. The ability of the model to predict the preheating and laser pulse shaping effects on crack distribution in weld pool were investigated and following results were obtained:

1- The solidification rate (r) distribution in the molten weld pool plays critical role in determination of the crack initiation site distribution. As the ratio of $(r_{WC}\text{-}r_{FL})/r_{FL}$ increases, the crack initiation sites will move toward the weld center.
2- In samples welded with a square-wave pulse, base metal preheating caused the majority of the solidification crack initiation sites to move from the FL to a location closer to the center of the weld pool. The results of the simulation show that, in comparison to welds made without preheating, $(r_{WC}\text{-}r_{FL})/r_{FL}$ increased because of the reduction in r_{FL}. The number of cracks also decreases along with the shifting of the crack initiation site as a result of $r \times l$ reduction due to decrease in r (despite an increase in l).
3- It was shown that ramp down pulse shaping was more effective compared to preheating at reducing cracks, as both r and l can be controlled and, in turn, $r \times l$ can be reduced enough to prevent crack initiation throughout the weld pool (i.e., $SCI < 0$ throughout the entire weld pool).
4- In comparison with the experimental findings on square-wave pulses, the proposed approach was able to predict and justify the trend change in crack initiation sites across the entire weld pool from monotonic decrease to nonlinear (increase and then decrease) distribution as a result of base metal preheating.

Appendix A

Gill et al. [28] reported that the solidification rate dependent liquidus slope (m_r) in Eq. (12) can be related to solidification rate dependent distribution coefficient (k_r) as follows:

$$m_r = m_0 \left[\frac{1 - k_r + k_r ln\left(\frac{k_r}{k_0}\right)}{1 - k_0} \right] \tag{23}$$

And similarly Sobolev [29] reported that C_L^* can also be stated as a function of k_r by:

$$C_L^* = \frac{C_0}{1 - \left(1 - k_r\right) Iv\left(P_C\right)} \tag{24}$$

$Iv\ (P_C)$ is Ivantsov function and P_C is the Peclet number of the solute diffusion at dendrite/cell tip. Peclet number was related to tip radius (r_t), the solute element diffusion coefficient in the liquid (D_L), and solidification rate (v) as follows:

$$P_C = \frac{r_t v}{2D_L} \tag{25}$$

It was proposed a local non-equilibrium diffusional model (LNDM) developed for the binary alloys rapid solidification conditions [29–31]. Based on this model, k_r can be calculated as a function of solidification rate (r), the solute element diffusive speed in the liquid (v_{Db}), and diffusive speed of the solute element across the interface (v_{Di}) by following equation.

$$k_v = \frac{k_0\left(1 - \frac{r^2}{v_{Db}^2}\right) + \frac{r}{v_{Di}}}{\left(1 - \frac{r^2}{v_{Db}^2}\right) + \frac{r}{v_{Di}}} \tag{26}$$

Reasonably based on this model when solidification rate reach to the speed of diffusive solute element in the liquid ($r = v_{Db}$) then $k_r = 1$, i.e., solute trapping at the interface occurs completely.

Appendix B

ΔT_E Can be computed using a model called TMK model [23]. TMK model showed that the parameters of ΔT_E at high solidification rates are dependent on r, as follows:

$$\Delta T_E = \frac{m_\alpha + m_\theta}{2}\left[\left[Z + \lambda\left(\partial Z/\partial\lambda\right)\right] \times \frac{2C_0 v}{f(1-f)D_L} \times \left(\frac{a_\alpha^L}{f m_\alpha} + \frac{a_\theta^L}{(1-f)m_\beta}\right)\right]^{1/2}\left(1 + \frac{Z}{P + \lambda\left(\partial Z/\partial\lambda\right)}\right) \tag{27}$$

are two series that can be related to the distribution coefficient at α/liquid interface (k_α), the Peclet number at the eutectic temperature (p), and f as follows:

$$Z = \sum_{n=1}^{\infty}\left(\frac{1}{n\pi}\right)^3 \sin^2(n\pi f) \times \frac{p_n}{\sqrt{1+p_n^2} - 1 + 2k_\alpha} \tag{28}$$

and

$$Z + \lambda\left(\partial Z/\partial\lambda\right) = \sum_{n=1}^{\infty}\left(\frac{1}{n\pi}\right)^3 sin^2(n\pi f) \times \left[\frac{p_n}{\sqrt{1+p_n^2} - 1 + 2k_\alpha}\right]^2 \frac{p_n}{\sqrt{1+p_n^2}} \tag{29}$$

Here, m_θ and m_α are the slopes of liquidus for θ and α phases. a_α^L and a_θ^L are the capillarity constants. C_0 is the eutectic tie-line length, f is the α phase volume fraction, and λ is the distance between the eutectic layer. P and $P + \lambda\left(\partial P/\partial\lambda\right)$

where

$$p_n = \frac{2n\pi}{p} \tag{30}$$

p can be stated as a function of the distance between eutectic layers (λ) [24] and the solute element diffusion coefficient in the liquid (D_L) by:

$$p = r\lambda/2D_L \tag{31}$$

Appendix C

The physical properties and constants for Al-Cu alloys that were used in this investigation are given in Table 6.

Table 6 Physical properties of Al (α)-Al_2Cu (θ) system required for calculations [24]

Parameter	Symbol	Value	Unit
Equilibrium distribution coefficient of α phase	k_α	0.17	-
Equilibrium distribution coefficient of θ phase	k_θ	0.05	-
Melting temperatures of pure aluminum	T_m	933.6,	K
Eutectic temperatures in Al-Cu alloys	T_E	821	K
Speed of solute diffusion across the S/ L interface for the phase α	v_{Di}	6.7	m/s
Speed of solute diffusion in the liquid bulk	v_{Db}	10.1	m/s
Composition of eutectic in Al-Cu alloy	C_E	32.7	wt.%
Volume fraction of the α-phase	f	0.54	-
Eutectic tie-line length	c_0	46.9	wt.%
Liquidus slope of α phase	m_α	− 3.4	K/wt%
Liquidus slope of θ phase	m_θ	2	K/wt%
Pre exponential constant	D_0	1.1×10^{-7}	m^2/s
Diffusion activation energy	Q	23.8	kJ/mol
Gibbs-Thompson constant for α phase	Γ_α	2.4×10^{-7}	K.m
Gibbs-Thompson constant for θ phase	Γ_θ	5.5×10^{-8}	K.m
Capillarity constant for α phase	a_α^L	2.2×10^{-7}	K.m
Capillarity constant for θ phase	a_θ^L	4.5×10^{-8}	K.m
Thermal gradient	G	5×10^6	K/m
Thermal conductivity in liquid	k_l	105	W/mK
Thermal conductivity in solid	k_s	210	W/mK

Author contribution Mohsen Sheikhi: investigation, writing. Zeinab Malekshahi Beiranvand: investigation. F. Malek Ghaini: advice. Michael J. Benoit: advice.

Availability of data and materials Not applicable.

Code availability Not applicable.

Declarations

Ethical approval The authors respect the Ethical Guidelines of the Journal.

Consent to participate Not applicable.

Consent to publication Not applicable.

Competing interests The authors declare no competing interests.

References

1. Coniglio N, Cross CE (2020) Effect of weld travel speed on solidification cracking behavior. Part 1: weld metal characteristics. Int J Adv Manuf Technol 107(11):5011–23
2. Coniglio N, Cross CE (2020) Effect of weld travel speed on solidification cracking behavior. Part 3: modeling. Int J Adv Manuf Technol 107(11):5039–51
3. Ghaini FM, Sheikhi M, Torkamany MJ, Sabbaghzadeh J (2009) The relation between liquation and solidification cracks in pulsed laser welding of 2024 aluminum alloy. Mater Sci Eng A 519(1–2):167–171
4. Michaud EJ, Kerr HW, Weckman DC (1995) Recent trends in welding science and technology, ASM International Congress, Gatlinburg, Tennessee, 153
5. Sheikhi M, Malek Ghaini F, Torkamany MJ, Sabbaghzadeh J (2009) Characterisation of solidification cracking in pulsed Nd: YAG laser welding of 2024 aluminium alloy. Sci Technol Weld Join 14(2):161–165
6. Eskin DG, Katgerman L (2004) Mechanical properties in the semi-solid state and hot tearing of aluminum alloys. Prog Mater Sci 49(5):629–711
7. Suyitno WH, Kool L (2005) Katgerman. Met Mater Trans A 36A:1537–1546
8. Coniglio N, Cross CE (2020) Effect of weld travel speed on solidification cracking behavior Part 2: testing conditions and metrics. Int J Adv Manuf Technol 107(11):5025–38
9. MalekshahiBeiranvand Z, MalekGhaini F, Sheikhi M, Abdollah-Zadeh A (2013) Effect of severe plastic deformation on hot cracking of wrought aluminium alloy in pulsed laser welding. Sci Technol Weld Join 18(6):473–477
10. Cross CE (2005) on the origin of weld solidification cracking. In: Boellinghaus T, Herold H (eds) Hot Cracking Phenomena in Welds. Springer
11. Sistaninia M, Phillionb AB, Drezeta J-M, Rappaz M (2012) Acta Mater 60:3902–3911
12. Kou S (2015) A criterion for cracking during solidification. Acta Mater 15(88):366–374
13. Easton MA, Gibson MA, Zhu S, Abbott TB (2014) An a priori hot-tearing indicator applied to die-cast magnesium-rare earth alloys. Metall and Mater Trans A 45(8):3586–3595
14. Rappaz M, Drezet J-M, Gremaud M (1999) Met Mat Trans A 30A:449–455
15. Braccini M, Martin CL, Suéry M, Bréchet Y (2000) Matér Techn 88:19–24
16. Suyitno WH, Katgerman L (2003) Evaluation of mechanical and non-mechanical hot tearing criteria for DC casting of an aluminum alloy. Light Met 2003:753–758
17. Sheikhi M, Ghaini FM, Assadi H (2015) Prediction of solidification cracking in pulsed laser welding of 2024 aluminum alloy. Acta Mater 82:491–502
18. M'hamdi M, Mo A, Martin CL (2002) Two-phase modeling directed toward hot tearing formation in aluminum direct chill casting. Metall Mater Trans A 33(7):2081–93
19. MJ-Aziz (1988) Mater Sci Eng 98:369–372
20. Coniglio N, Cross CE (2009) Mechanisms for solidification crack initiation and growth in aluminum welding. Metall Mater Trans A 40(11):2718–2728
21. Fabregue D, Deschamps A, Suery M, Poole WJ (2006) Rheological behavior of Al-Mg-Si-Cu alloys in the mushy state obtained by partial remelting and partial solidification at high cooling rate. Metall Mater Trans A 37(5):1459–1467
22. Katayama S, Mizutani M, Matsunawa A (1997) Modelling of melting and solidification behaviour during laser spot welding. Sci Technol Weld Join 2(1):1–9
23. Trivedi R, Magnin P, Kurz W (1987) Theory of eutectic growth under rapid solidification conditions. Acta Metall 35(4):971–980
24. Zimmermann M, Carrad M, Kurz W (1989) Acta Mater 37:3305–3313
25. Jia Z, Zhang P, Yu Z, Shi H, Liu H, Wu D, Ye X, Wang F, Tian Y (2021) Effect of pulse shaping on solidification process and crack in 5083 aluminum alloy by pulsed laser welding. Opt Laser Technol 134:106608
26. von Witzendorff P, Kaierle S, Suttmann O, Overmeyer L (2015) Using pulse shaping to control temporal strain development and solidification cracking in pulsed laser welding of 6082 aluminum alloys. J Mater Process Technol 225:162–169
27. Von Witzendorff P, Kaierle S, Suttmann O, Overmeyer L (2015) In situ observation of solidification conditions in pulsed laser welding of AL6082 aluminum alloys to evaluate their impact on hot cracking susceptibility. Metall Mater Trans A 46(4):1678–1688
28. Gill SG, Kurz W (1995) Acta Mater 43:139–151
29. Sobolev SL (2016) A novel hybrid model combining continuum local nonequilibrium and discrete variables methods for solute trapping during rapid alloy solidification. Acta Mater 116:212–218
30. MalekshahiBeiranvand Z, MalekGhaini F, NaffakhMoosavy H, Sheikhi M, Torkamany MJ (2019) An analytical model for prediction of solidification cracking susceptibility in aluminum alloys taking into account the effect of solidification rate. Metall Mater Trans A 50(6):2835–2846
31. Beiranvand ZM, Ghaini FM, Moosavy HN, Sheikhi M, Torkamany MJ (2019) Solidification cracking susceptibility in pulsed laser welding of Al–Mg alloys. Materialia 7:100417